

Perfect one-dimensional interface states in a twisted stack of three-dimensional topological insulators

Manato Fujimoto, Takuto Kawakami, and Mikito Koshino
Department of Physics, Osaka University, Osaka 560-0043, Japan
 (Dated: June 28, 2022)

We theoretically study the electronic structure of interface states in twisted stacks of three-dimensional topological insulators. When the center of the surface Dirac cone is located at a midpoint of a side of BZ boundary, we find that an array of nearly-independent one-dimensional channels is formed by the interface hybridization of the surface states, even when the moiré pattern itself is isotropic. The two counter-propagating channels have opposite spin polarization, and they are robust against scattering by spin-independent impurities. The coupling between the parallel channels can be tuned by the twist angle. The unique 1D states can be understood as effective Landau levels where the twist angle works as a fictitious magnetic field.

I. INTRODUCTION

Moiré superlattices, formed by stacking two dimensional (2D) materials with a small twist angle or lattice mismatch, have become a topic of great interest in condensed matter physics. In these materials, [1–24] highly tunable electronic structures by twist angle serve as platforms to search for novel exotic phenomena. In a low-angle twisted bilayer graphene, in particular, Dirac fermions of intrinsic graphenes are strongly hybridized into nearly-flat bands [25–36], leading to strongly correlated phenomena such as superconductivity and strongly correlated insulating states. Moiré superlattices have been studied in a wide variety of 2D materials, including twisted multilayer graphenes [5–7, 16, 17], transition metal dichalcogenides [2, 4, 9–11, 23], 2D magnets [18–21] and semiconductors [1, 12–14].

The exploration of moiré physics was also extended to three-dimensional topological insulators (3DTIs), which contain two-dimensional Dirac fermions on the surface. For instance, the moiré pattern was observed on misaligned topmost quintuple layers of Bi_2Se_3 [37] and Bi_2Te_3 [38], and the electronic property in such a system was theoretically studied. [39] Previous theoretical works also investigated a 3DTI modulated by 2D materials placed on the surface [40], and topological phases in a twisted bilayer of $\text{Bi}_2(\text{Te}_{1-x}\text{Se}_x)_3$. [41]

Here we ask: when a pair of 3DTI slabs are overlapped on top of each other with a twist angle, how the surface Dirac cones would interact. One may think that physics would be similar to the twisted bilayer graphene, which also have Dirac cones with moiré interface coupling. In this paper, on contrary to the expectation, we demonstrate that the interface band structures are completely different depending on the position of the Dirac cone in the Brillouin zone (BZ). Generally, the center of the surface Dirac cone is located at a time reversal invariant momentum (TRIM). When the TRIM is at Γ point, the surface states are found to be simply gapped out in a twisted interface. When the TRIM is at a corner point of BZ, a flat band similar to twisted bilayer graphene is realized. [42]

When the TRIM is at a midpoint of a side of BZ boundary, on the other hand, we find that the surface Dirac cones of top and bottom surfaces are converted to a perfect 1D channel as depicted in Fig. 1(a), which is completely flat in one direction while disperses in the other direction. There, the left-going and right-going modes have opposite spin textures [Fig. 1(b)], and they are robust against scattering by spin-independent impurities. Moreover, these peculiar 1D bands can be analytically understood as Landau levels of a formally equivalent lattice model, where the twist angle works as a fictitious magnetic field. The 1D bands are formed when the twist angle is sufficiently small, and there is no magic angle condition to have the 1D channels. The theory is applicable to the side-centered surface Dirac cones found in SnTe (111) surface. [43–45] The interaction between 1D channels can be tuned by the twist angle, and it would be an ideal platform to study weakly-coupled Tomonaga-Luttinger liquid [19, 46–57].

The paper is organized as follows. In Sec. II, we introduce a continuum model of twisted 3DTIs based on the symmetry consideration. In Sec. III, we calculate the energy spectrum for the M-centered model, and we describe the emergence of the spin polarized 1D propagation mode by a pseudo-Landau description. A brief conclusion is given in Sec. IV.

II. EFFECTIVE CONTINUUM MODEL

We construct a twisted 3DTI stack in the following procedures. We consider a pair of the same kind of 3DTI slabs shown in Fig. 2(a). We set xy plane on the surface, and z axis perpendicular to it. We assume the individual 3DTI slabs (before twisting) have (1) time reversal symmetry \mathcal{T} and (2) mirror symmetries of \mathcal{M}_x (with respect to yz -plane) and \mathcal{M}_y (zx -plane). We flip one slab and stack it on the top of the other, such that the two slabs share the same mirror planes [Fig. 2(b)]. Then we twist the top and bottom slabs with respect the z -axis by angle $\pm\theta/2$, respectively, and finally obtain a twisted 3DTI system [Fig. 2(c)]. The entire system has time reversal sym-

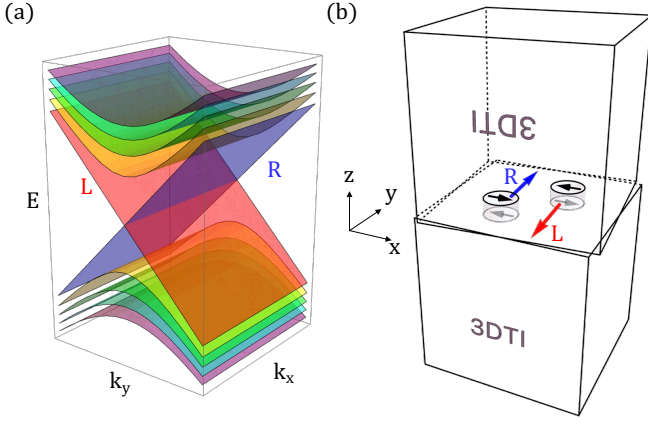


FIG. 1: (a) Band structure of the interface states in twisted 3DTIs with the TRIM at a midpoint of the Brillouin zone boundary. The energy bands are completely flat in k_x , while disperse in k_y direction. “L” and “R” represent linear bands with left-going and right-going band velocities. (b) Schematic picture of L and R states where red and blue arrows indicate the corresponding band velocities, and black arrows represent spin directions in upper and lower 3DTI’s surfaces.

metry and two-fold rotation symmetries along x, y, z axes, C_{2x}, C_{2y}, C_{2z} . In Appendix B, we also present the consideration of 3DTIs with lower spatial symmetries where individual slabs respect only either \mathcal{M}_x or \mathcal{M}_y , where we will see that the basic properties are not changed.

At the interface, the surface states of the individual TIs are coupled by the moiré interlayer coupling. We derive an effective continuum model to describe these hybrid surface modes. The Hamiltonian is generally written as

$$H = \begin{pmatrix} H_u & H_{\text{int}}^\dagger \\ H_{\text{int}} & H_l \end{pmatrix}, \quad (1)$$

where $H_{u/l}$ is the surface Dirac Hamiltonian of the upper and lower TIs, respectively, and H_{int} describes the interface coupling.

We determine the form of $H_{u/l}$ and H_{int} from the symmetry consideration without specifying a microscopic model. For the intra-surface part, $H_{u/l}$, the center of the surface Dirac cone is generally located at time reversal invariant momentum (TRIM) Λ in the BZ. In this paper, we consider two distinct cases where the TRIM is Γ point ($\Lambda = 0$) and M point (the midpoint of a side of the BZ boundary). From the symmetry constraints ($\mathcal{T}, \mathcal{M}_x, \mathcal{M}_y$), the surface Dirac Hamiltonian $H_{u/l}$ before the twist is written in the lowest order in k as

$$H_{u/l} = \pm(v_x s_2 k_x - v_y s_1 k_y), \quad (2)$$

where \pm are for u and l , respectively, $v_{x/y}$ is the band velocity in x/y direction, $\mathbf{k} = (k_x, k_y)$ is two-dimensional momentum, and s_i ($i = 1, 2, 3$) is the Pauli matrices for spin degree of freedom. The derivation for Eq. (2) is given in Appendix A. In the following, we assume an

isotropic surface Dirac cone $v_x = v_y (\equiv v)$ for simplicity, while anisotropy does not much affect qualitative results as shown in Appendix B3.

In the twisted TI stack, the TRIM is shifted to $R(\pm\theta/2)\Lambda$ where $R(\alpha)$ is the rotation matrix on the surface plane by angle α . The location of the TRIMs are as illustrated in Fig. 3(a) and (b) for the trigonal/hexagonal and the tetragonal cases, respectively. Note that M_1, M_2, \dots are distinct points. While the mid-points on the BZ boundary in the tetragonal system are usually labelled by X and Y , we use symbol M regardless of the crystal symmetry through out the paper. The intra-surface Hamiltonians $H_{u/l}$ of the twisted TI stack (relative to the shifted TRIMs) are given by (2) even after rotation, as long as $v_x = v_y$ is assumed.

The interface-coupling Hamiltonian H_{int} can be obtained from the following consideration. Let \mathbf{b}_i ($i = 1, 2$) the reciprocal lattice vectors of the 3DTI without rotation. In the extended zone scheme, the equivalent points of Λ are written as

$$\Lambda_{n_1, n_2} = \Lambda + n_1 \mathbf{b}_1 + n_2 \mathbf{b}_2, \quad (3)$$

where n_1 and n_2 are integers. In the twisted TI stack, they are shifted to

$$\Lambda_{n_1, n_2}^\pm = R(\pm\theta/2)\Lambda_{n_1, n_2}. \quad (4)$$

Figure 4 shows the points of Λ_{n_1, n_2}^\pm for Γ , M_1 and K point in the hexagonal lattice, where red and black points represent \pm , respectively. Note that K is not a TRIM, but it is relevant to consider the interlayer coupling of twisted bilayer graphene and here we include it for comparison. At each (n_1, n_2) , we can define an interlayer shift as

$$\mathbf{q}_{n_1, n_2} = \Lambda_{n_1, n_2}^+ - \Lambda_{n_1, n_2}^-. \quad (5)$$

When θ is small, the interface Hamiltonian is approximately given by [58]

$$H_{\text{int}} = \sum_{n_1, n_2} T(\Lambda_{n_1, n_2}) \exp(i\mathbf{q}_{n_1, n_2} \cdot \mathbf{r}), \quad (6)$$

where $T(\mathbf{k})$ is a 2×2 matrix. In the tight-binding approach, $T(\mathbf{k})$ is essentially the Fourier transform of the distance-dependent interlayer transfer integral in the real space, and therefore its amplitude rapidly decays in increasing $|\mathbf{k}|$. [58] The interface coupling Eq. (6) can be intuitively understood by using the diagram of Fig. 4. For each pair of black and red dots ($\Lambda_{n_1, n_2}^+, \Lambda_{n_1, n_2}^-$), the relative position \mathbf{q}_{n_1, n_2} represents the shift of the Dirac-cone centers, and the distance from the origin (i.e., Λ_{n_1, n_2}) determines the coupling amplitude, where a further distance corresponds to a smaller coupling.

In this paper, we only take the nearest black-red pair(s) within the first BZ, which gives a dominant contribution. For Γ point [$\Lambda = 0$, Fig. 4(a)], for instance, we only take the central pair with a shift of $\mathbf{q} = 0$. For M_1 point [Fig. 4(b)], we have two pairs at same distance from the origin, which have the shift vectors of

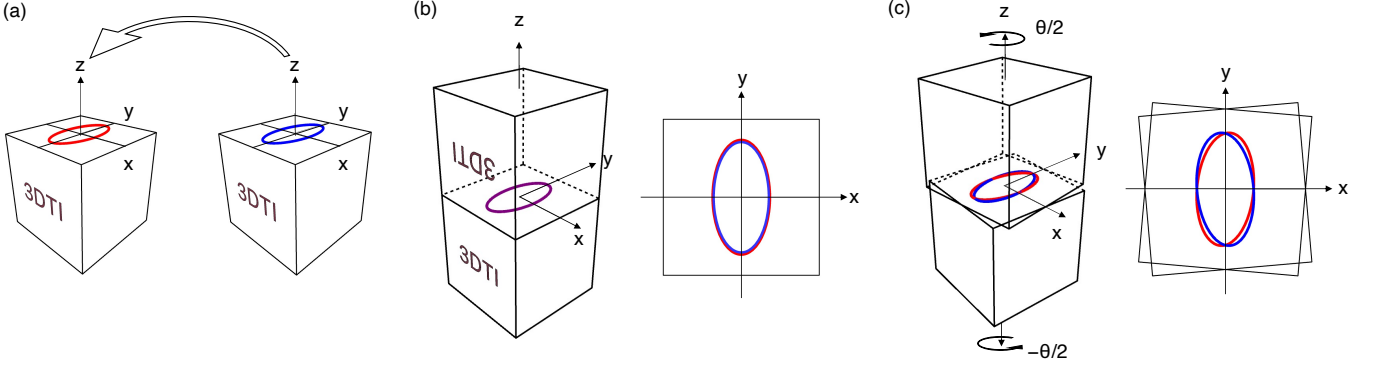


FIG. 2: Construction of a twisted 3DTI stack. (a) A pair of identical 3DTI slabs. An ellipsoid on each surface represents the mirror symmetries M_x and M_y . (b) Non-twisted 3DTI stack. One slab is flipped over and stacked on the other such that the two slabs share the same mirror planes. (c) Twisted 3DTI stack with the twist angle θ .

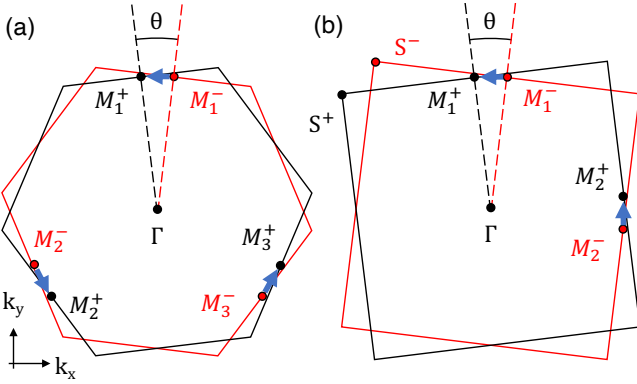


FIG. 3: The first BZs and TRIMs of (a) trigonal/hexagonal and (b) tetragonal crystals twisted by $\pm\theta/2$. The TRIMs are shown as dots.

$\mathbf{q} = \pm\mathbf{q}_\theta$, where $\mathbf{q}_\theta = [R(\theta/2) - R(-\theta/2)]\mathbf{M}_1$. For K point [Fig. 4(c)], there are the three nearest pairs with shifts of $\mathbf{q} = \mathbf{q}_\theta^1, \mathbf{q}_\theta^2, \mathbf{q}_\theta^3$, where $\mathbf{q}_\theta^j = R[2\pi(j-1)/3]\Delta\mathbf{K}$ and $\Delta\mathbf{K} = [R(\theta/2) - R(-\theta/2)]\mathbf{K}$. The coupling of the upper and lower surface Dirac cones with the shift vectors are illustrated in the lower panels of Fig. 4. The Γ -point case [Fig. 4(d)] only has an interlayer coupling with $\mathbf{q} = 0$, i.e. no spatial modulation. The M -point case [Fig. 4(e)] only gives a one-dimensional coupling with $\mathbf{q} = \pm\mathbf{q}_\theta$. The K -point case [Fig. 4(f)] corresponds to the twisted bilayer graphene[30–36, 58], where three shift vectors $\mathbf{q}_\theta^1, \mathbf{q}_\theta^2, \mathbf{q}_\theta^3$ give a two-dimensional superlattice coupling of the Dirac cones.[30–36, 58]

The specific form of H_{int} can be obtained by the symmetry consideration as follows. First let us consider the Γ -point centered case, where the interface-coupling Hamiltonian is given by a constant matrix $H_{\text{int}}^{(\Gamma)} = T$ (independent of the position \mathbf{r}) as argued. For the Hamiltonian of twisted TI, Eq. (1), the symmetry operators are expressed as $\mathcal{T} = is_2\mathcal{K} \otimes \tau_0$, $C_{2x} = is_1 \otimes \tau_1$ and

$C_{2y} = is_2 \otimes \tau_1$, where \mathcal{K} is the complex conjugate operator and τ_i is the Pauli matrix for u/l degree of freedom. We require that Eq. (1) respects these symmetries, or

$$\begin{aligned} \mathcal{T}H(\mathbf{k}, \mathbf{r})\mathcal{T}^{-1} &= H(-\mathbf{k}, \mathbf{r}), \\ C_{2x}H(\mathbf{k}, \mathbf{r})C_{2x}^{-1} &= H(C_{2x}\mathbf{k}, C_{2x}\mathbf{r}), \\ C_{2y}H(\mathbf{k}, \mathbf{r})C_{2y}^{-1} &= H(C_{2y}\mathbf{k}, C_{2y}\mathbf{r}), \end{aligned} \quad (7)$$

where \mathbf{k} and \mathbf{r} are 2D vectors on the interface plane. Then the inter-surface submatrix H_{int} is forced to have the form,

$$H_{\text{int}}^{(\Gamma)} = t_0s_0 + it_3s_3, \quad (8)$$

where t_0 and t_3 are real numbers. The entire Hamiltonian is written as

$$H^{(\Gamma)} = v(s_2k_x - s_1k_y) \otimes \tau_3 + t_0s_0 \otimes \tau_1 + t_3s_3 \otimes \tau_2, \quad (9)$$

giving the eigenvalues $E = \pm(v^2k^2 \pm 2t_3vk + t_0^2 + t_3^2)^{1/2}$. Therefore, the Dirac cones obtain an energy gap of the magnitude of $(t_0^2 + t_3^2)^{1/2}$. This is a trivial result naturally expected when the same kind of TIs are overlapped.

When the surface Dirac cone is located at M_1 as shown in Fig. 3, on the other hand, the interface-coupling Hamiltonian takes the form of $H_{\text{int}}^{(M_1)} = T(\mathbf{M}_1)e^{i\mathbf{q}_\theta \cdot \mathbf{r}} + T(-\mathbf{M}_1)e^{-i\mathbf{q}_\theta \cdot \mathbf{r}}$. By requiring that Eq. (1) respects $\mathcal{T}, C_{2x}, C_{2y}$, the interface Hamiltonian Eq. (6) is reduced to

$$\begin{aligned} H_{\text{int}}^{(M_1)} &= T_+e^{i\mathbf{q}_\theta \cdot \mathbf{r}} + T_-e^{-i\mathbf{q}_\theta \cdot \mathbf{r}}, \\ T_{\pm} &= t_0s_0 \pm t_2s_2 + it_3s_3, \end{aligned} \quad (10)$$

where t_0, t_2, t_3 are real numbers. As we will see in the following section, this results in a completely different band structure with nearly perfect one-dimensional modes.

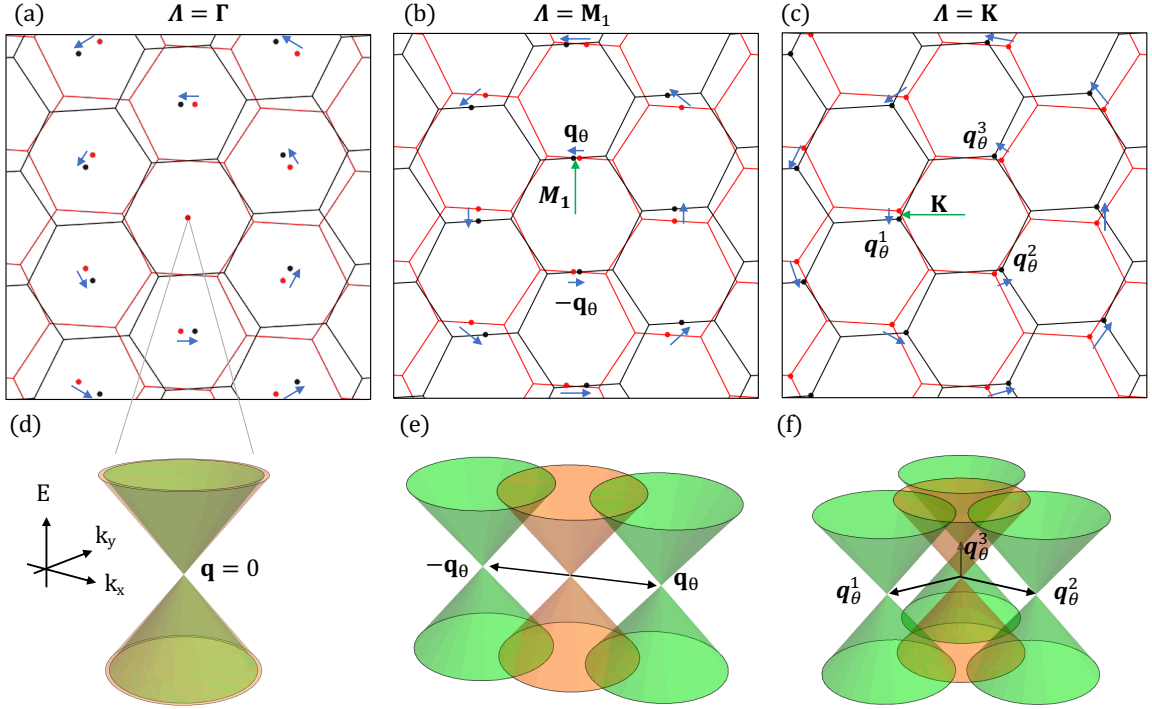


FIG. 4: Equivalent points of (a) Γ , (b) M_1 , (c) K in the twisted hexagonal BZs in the extended zone scheme. The red and black dots represent Λ_{n_1, n_2}^\pm [Eq. (4)], and the blue arrows are the momentum shift vector \mathbf{q}_{n_1, n_2} [Eq. (5)]. Lower panels (d)-(f) illustrate the coupling of the upper and lower Dirac cones with the dominant momentum shifts in (a)-(c), respectively.

III. PERFECT 1D STATES IN M-POINT 3DTI

A. Band structure

We calculate the band structure of the twisted 3DTIs with the surface Dirac cone at M_1 . Following the argument in the previous section, we consider the Hamiltonian,

$$H = \begin{pmatrix} H_u(\mathbf{k}) & H_{\text{int}}^{(M_1)^\dagger} \\ H_{\text{int}}^{(M_1)} & H_l(\mathbf{k}) \end{pmatrix}, \quad (11)$$

where $H_{u/l}(\mathbf{k}) = \pm v(s_2 k_x - s_1 k_y)$, and $H_{\text{int}}^{(M_1)}$ is given by (10). By arranging the wave bases as $\{\cdots, |\mathbf{k}_{-1} \uparrow\rangle, |\mathbf{k}_{-1} \downarrow\rangle, |\mathbf{k}_0 \uparrow\rangle, |\mathbf{k}_0 \downarrow\rangle, |\mathbf{k}_1 \uparrow\rangle, |\mathbf{k}_1 \downarrow\rangle, \cdots\}$ where $\mathbf{k}_n = \mathbf{k} + n\mathbf{q}_\theta$, the Hamiltonian matrix is written as

$$H = \begin{pmatrix} \ddots & & & & & & \\ H_u(\mathbf{k}_{-2}) & T_+^\dagger & & & & & \\ T_+ & H_l(\mathbf{k}_{-1}) & T_- & & & & \\ & T_-^\dagger & H_u(\mathbf{k}_0) & T_+^\dagger & & & \\ & & T_+ & H_l(\mathbf{k}_1) & T_- & & \\ & & & T_-^\dagger & H_u(\mathbf{k}_2) & & \\ & & & & \ddots & & \end{pmatrix}, \quad (12)$$

with T_\pm defined in Eq. (10). This describes one-dimensional coupling in a series of the Dirac cones illustrated in Fig. 4(e). Here we set $\mathbf{q}_\theta = (q_\theta, 0)$, so that the moiré BZ is given by $-q_\theta/2 \leq k_x \leq q_\theta/2$, while unbounded in k_y direction. The q_θ is related to the twist angle by

$$q_\theta = 2M_1 \sin \frac{\theta}{2} \approx M_1 \theta, \quad (13)$$

where M_1 is the distance from Γ to M_1 .

We numerically calculate band structure by truncating the series with a sufficiently large $|n|$, and diagonalizing the Hamiltonian matrix. We have three real parameters, t_0, t_2, t_3 in the interface Hamiltonian. First we consider the simplest case with $t_2 = t_3 = 0$. The system is characterized by a dimensionless wavenumber $q_\theta/(t_0/v)$, which is proportional to the twist angle θ . In Figs. 5 (a), (b) and (c), we plot the band structures for $q_\theta = 1.5, 0.75, 0.25(t_0/v)$ with $t_2 = t_3 = 0$, where the left and right hand sides of each panel show the band dispersions along k_x and k_y axes, respectively, with the origin taken at M_1^+ . For k_x , we take the extended zone scheme where the BZ boundaries are indicated by vertical lines.

We see that the interface coupling opens a band gap at every crossing point of different Dirac cones, whereas the energy bands at M_1^\pm remain doubly degenerate, which are the Kramers doublets. In decreasing q_θ (decreasing twist angle), the low-lying bands are flattened in k_x axis,

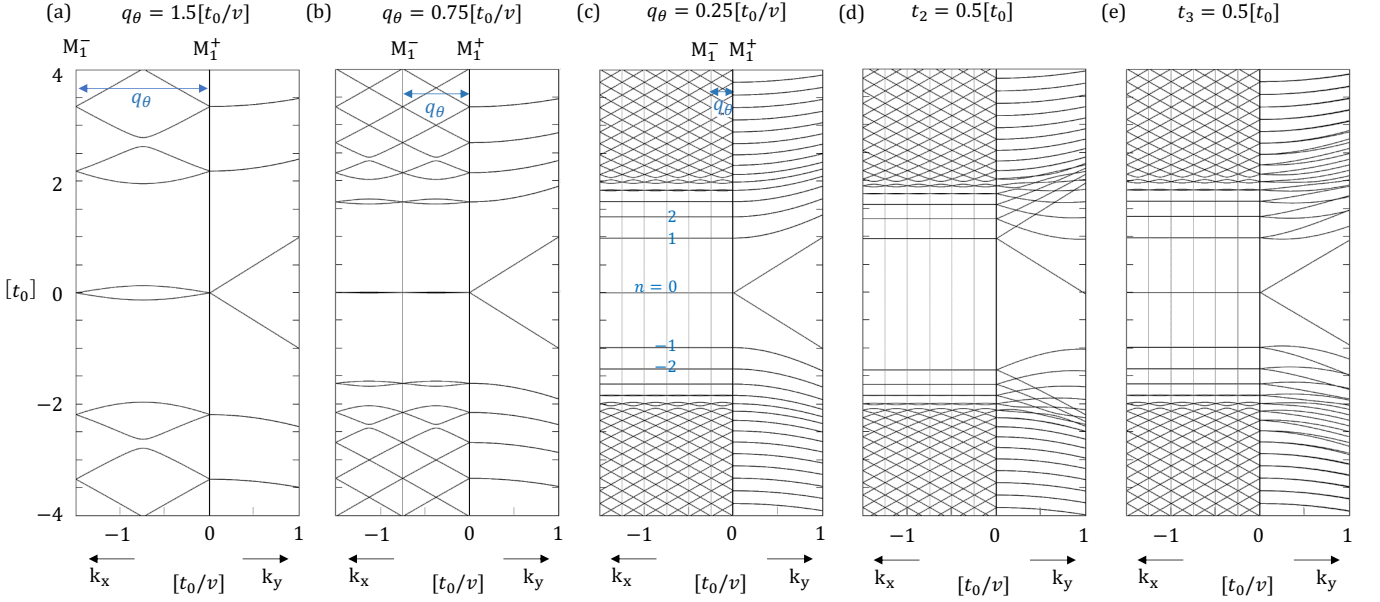


FIG. 5: Band structure of the twisted 3DTIs with the surface Dirac cone at M_1 , calculated for different twist angles of (a) $q_\theta = 1.5$, (b) 0.75 , (c) 0.25 (in units of t_0/v) with $t_2 = t_3 = 0$, and for different band parameters (d) $(t_2, t_3) = (0.5t_0, 0)$ and (e) $(0, 0.5t_0)$ with $q_\theta = 0.25$. The left and right hand sides of each panel show the band dispersions along k_x and k_y axes, respectively, with respect to M_1^\pm . For k_x , we take the extended zone scheme where the BZ boundaries are indicated by vertical lines.

while the dispersion along k_y remains intact. The entire band structure on $k_x k_y$ plane is illustrated in Fig. 1(a), showing a nearly-perfect 1D bands which disperses only in the y direction. If we have inequivalent M_j points as in Fig. 3, each valley contributes to such a 1D band which disperses in parallel to the line $\Gamma - M_j$, while the bands of different M_j 's are not hybridized as long as the moiré period is much greater than the atomic scale. Anisotropic band flattening in a moiré system with a base momentum at the BZ edge was also argued in a previous work from a crystallographic point of view.[59]

We label the 1D subbands as $n = 0, \pm 1, \pm 2, \dots$, as Fig. 5(c). In $k_y = 0$, each level is doubly degenerate due to the Kramers doublet at M_1^\pm and the band flattening. The energy of the $\pm n$ -th band in $k_y = 0$ approximates $\pm \sqrt{4t_0 v q_\theta |n|}$, which is analogous to the Landau levels of monolayer graphene.[60–62] Actually there is a formal mapping of the Hamiltonian of twisted 3DTIs [Eq. (12)] to a 2D Dirac Hamiltonian under a magnetic field, which will be argued in the next section.

We plot the band structure with nonzero t_2 and t_3 in

Fig. 5(d) and (e), respectively, at the same q_θ as in Fig. 5(c). The t_2 works like a mass in the graphene's Landau level shifting $n = 0$ level by $2t_2$, and also splits the double degeneracy in $k_y \neq 0$. The t_3 hardly changes the band energies of $k_y = 0$, while it only splits the double degeneracy in $k_y \neq 0$. These features can also be explained by the mapping to the Landau levels.

B. Pseudo-Landau level description for 1D interface modes

To understand the 1D dispersion argued in the previous section, we introduce a formal mapping between the M -centered twisted 3DTIs [Eq. (12)] and a 2D Dirac Hamiltonian under a magnetic field. First, we apply a spin rotation to Eq. (12) which replaces spin Pauli matrices as

$$(s_1, s_2, s_3) \rightarrow (s_2, s_3, s_1). \quad (14)$$

As a result, the Hamiltonian matrix becomes,

$$H = \begin{pmatrix} \ddots & & & & & & & \\ & \epsilon_{-1} & t_0 - t_2 & & & & & \\ & t_0 - t_2 & \epsilon_0 & t_0 + t_2 & & & & \\ & & t_0 + t_2 & \epsilon_{+1} & & & & \\ & & & & \ddots & & & \\ \hline \ddots & & & & & & & \\ & ivk_y & it_3 & & & & & \\ & -it_3 & -ivk_y & -it_3 & & & & \\ & & it_3 & ivk_y & & & & \\ & & & & \ddots & & & \\ \hline \ddots & & & & & & & \\ & -\epsilon_{-1} & t_0 + t_2 & & & & & \\ & t_0 + t_2 & -\epsilon_0 & t_0 - t_2 & & & & \\ & & t_0 - t_2 & -\epsilon_{+1} & & & & \\ & & & & \ddots & & & \end{pmatrix}, \quad (15)$$

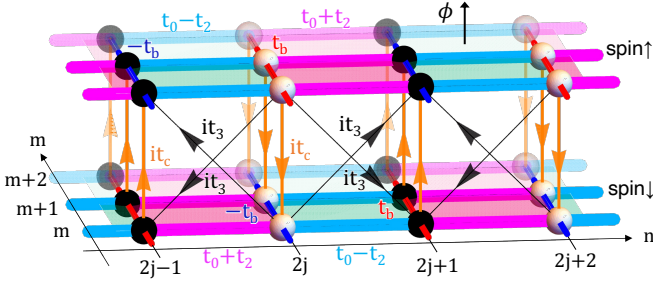


FIG. 6: The square-lattice model for Eq. (16). The top and bottom layer represent $s_3 = \pm 1$, respectively. The unit cell includes a black and white site for each layer. The normal lines indicate real hopping while the arrows indicate imaginary hopping.

where the upper and lower blocks represent $s_3 = \pm 1$ sectors, respectively, and $\epsilon_n = (-1)^n v(k_x + nq_\theta)$. Note that $s_3 = \pm 1$ now represent spin polarization in $\pm y$ direction, which is parallel to the propagating direction of the 1D interface modes.

Now we show that the Hamiltonian of Eq. (15) is equivalent to a square-lattice fermion model under a magnetic field, as illustrated in Fig. 6. Here the top and bottom layers represent spin degree of freedom $s = \uparrow, \downarrow$ (corresponds to $s_3 = \pm 1$ in Eq. (15)), respectively. The lattice points on the square grid are labeled by (n, m) , where the

lattice spacing is 1. The system is subjected to magnetic flux ϕ per 1×1 plaquette perpendicular to the lattice plane. The Hamiltonian is written as

$$\begin{aligned} \mathcal{H} = & \sum_{n,m} \sum_{s=\uparrow,\downarrow} \left[[t_0 + s(-1)^n t_2] c_{n+1,m,s}^\dagger c_{n,m,s} \right. \\ & \left. + s(-1)^n t_b e^{2\pi i n \phi} c_{n,m+1,s}^\dagger c_{n,m,s} \right] \\ & + \sum_{n,m} \left[(-1)^n (-it_c) c_{n,m,\uparrow}^\dagger c_{n,m,\downarrow} \right. \\ & \left. + (-1)^n it_3 (c_{n+1,m,\uparrow}^\dagger c_{n,m,\downarrow} + c_{n-1,m,\uparrow}^\dagger c_{n,m,\downarrow}) \right] \\ & + h.c. \end{aligned} \quad (16)$$

where $c_{n,m,s}^\dagger$ and $c_{n,m,s}$ are creation and annihilation operators of a fermion at the site (n, m) with spin s . The variable s in the equation is regarded as ± 1 for $s = \uparrow, \downarrow$. The parameters t_0, t_2, t_3, t_b, t_c are all set to be real. The hopping integrals except for t_0 are staggered in the n direction. The effect of the magnetic flux ϕ is incorporated as the Peierls phase in the hopping of t_b .

The Hamiltonian of Eq. (16) is periodic along m , so that the eigenstates can be written as $\Psi_{n,m,s} = e^{ik_b m} \psi_{n,s}$. The Hamiltonian matrix for the wavefunction $(\cdots \psi_{-1,\uparrow}, \psi_{0,\uparrow}, \psi_{1,\uparrow}, \cdots | \cdots \psi_{-1,\downarrow}, \psi_{0,\downarrow}, \psi_{1,\downarrow}, \cdots)$ is written as

$$\begin{pmatrix}
\ddots & & & & & \\
& +\lambda_{-1} & t_0 - t_2 & & & \\
& t_0 - t_2 & +\lambda_0 & t_0 + t_2 & & \\
& & t_0 + t_2 & +\lambda_{+1} & & \\
& & & & \ddots & \\
\hline
& & & & & \\
& \ddots & & & & \\
& & -it_c & it_3 & & \\
& & -it_3 & it_c & & \\
& & & it_3 & -it_c & \\
& & & & it_c & \\
& & & & & \ddots
\end{pmatrix}
\begin{pmatrix}
\ddots & & & & & \\
& it_c & it_3 & & & \\
& -it_3 & -it_c & -it_3 & & \\
& & it_3 & it_c & & \\
& & & & \ddots & \\
\hline
& & & & & \\
& \ddots & & & & \\
& & -\lambda_{-1} & t_0 + t_2 & & \\
& & t_0 + t_2 & -\lambda_0 & t_0 - t_2 & \\
& & & t_0 - t_2 & -\lambda_{+1} & \\
& & & & & \ddots
\end{pmatrix}
\quad (17)$$

Lattice model	Twisted 3DTIs
$2t_b$	v
t_c	$-vk_y$
$2\pi\phi$	$q\theta$
k_b	k_x
t_0, t_2, t_3	t_0, t_2, t_3
spin (s_i)	spin (s_i) [After Eq. (14)]
$n = 2j, 2j+1$ (τ_i)	top / bottom surfaces (τ_i)

TABLE I: Correspondence of parameters between the effective lattice model and the twisted 3DTIs.

where $\lambda_n = 2t_b(-1)^n \cos(2\pi\phi n + k_b)$. If the magnetic flux is much smaller than 1, λ_n is approximated by $2t_b(-1)^n(k_b + 2\pi n\phi)$ in the vicinity of $k_b = \pi/2$. We immediately see that Eq. (17) is formally equivalent to Eq. (15), under a relationship shown in Table I. Therefore, the 1D surface states in 3DTI are mapped to the Landau levels of the lattice fermion model of Eq. (16).

Actually, the Landau levels of the lattice model can be analytically expressed by the low-energy approximation as follows. First, we show that the model of Eq. (16) in zero magnetic flux has Dirac bands in the low-energy region. In $\phi = 0$, a unit cell is given by a 2×1 square in the (n, m) grid. The corresponding Bloch Hamiltonian is written as

$$\begin{aligned}
H(\mathbf{k}) = & 2t_0 \cos k_a (s_0 \otimes \tau_1) + 2t_2 \sin k_a (s_3 \otimes \tau_2) \\
& + 2t_b \cos k_b (s_3 \otimes \tau_3) + t_c (s_2 \otimes \tau_3) + 2t_3 \cos k_a (s_1 \otimes \tau_2),
\end{aligned}
\quad (18)$$

where s_i is the Pauli matrix for the spin degree of freedom, and τ_i is that for the sublattice pseudospin of $n = 2j, 2j+1$, which corresponds to the top / bottom surfaces of the twisted 3DTIs [Eq. (15)]. The $\mathbf{k} = (k_a, k_b)$ is the Bloch wave vectors for (n, m) space, and the BZ is given by $-\pi/2 \leq k_a \leq \pi/2$ and $-\pi \leq k_b \leq \pi$, in accordance with the 2×1 unit cell.

The energy spectrum of Eq. (18) has independent massive Dirac bands at $(k_a, k_b) = (\pi/2, \pm\pi/2)$. We choose $\mathbf{k}_0 = (\pi/2, \pi/2)$ and expand Eq. (18) with respect to \mathbf{k}_0 . Since $H(\mathbf{k})$ commutes with $s_1\tau_1$ when $t_3 = 0$, we block-

diagonalize the Hamiltonian into $s_1\tau_1 = \pm 1$ sectors by a unitary transformation. Specifically, we take the basis of $U = (\mathbf{u}_1^\dagger, \mathbf{u}_2^\dagger, \mathbf{u}_1^-, \mathbf{u}_2^-)$, where

$$\mathbf{u}_1^\pm = (z, \mp z^*, -z^*, \pm z)^T, \quad \mathbf{u}_2^\pm = (-z^*, \pm z, z, \mp z^*)^T, \quad (19)$$

with $z = (1 + i)/(2\sqrt{2})$, and four components in each vector represent wave amplitudes of $(\tau_3, s_3) = (+, +), (+, -), (-, +), (-, -)$. The \mathbf{u}_i^\pm corresponds to $s_1\tau_1 = \pm 1$, respectively. The transformed Hamiltonian reads

$$U^\dagger H(\mathbf{k}) U = \begin{pmatrix} h_+ & 2it_3 k_a \sigma_2 \\ -2it_3 k_a \sigma_2 & h_- \end{pmatrix}, \quad (20)$$

with

$$h_\pm = -2t_0 k_a \sigma_1 + 2t_b k_b \sigma_2 + M_\pm \sigma_3, \quad M_\pm = 2t_2 \pm t_c, \quad (21)$$

where h_\pm is for $s_1\tau_1 = \pm 1$, and σ_i the Pauli matrix for the degree of freedom in each sector. Obviously h_\pm are 2D massive Dirac Hamiltonians.

The Landau levels in a magnetic flux ϕ can be obtained by replacing momentum (k_a, k_b) with magnetic momentum (π_a, π_b) , which satisfies a commutative rule $[\pi_a, \pi_b] = -2\pi i\phi$. By using ladder operators a and a^\dagger which satisfy $[a, a^\dagger] = 1$, the magnetic momentum can be expressed as

$$(\pi_a, \pi_b) = \left(-\frac{\Delta}{4t_0} (a^\dagger + a), -\frac{\Delta}{4it_b} (a^\dagger - a) \right), \quad (22)$$

where $\Delta = \sqrt{16\pi t_b t_0 \phi}$. Then the Hamiltonian h_\pm becomes

$$h_\pm = \begin{pmatrix} M_\pm & \Delta a^\dagger \\ \Delta a & -M_\pm \end{pmatrix}. \quad (23)$$

When $t_3 = 0$, the energies of the Landau levels are given by the eigenvalues of h_\pm , or

$$E_{n,\pm} = \begin{cases} M_\pm & (n = 0) \\ \text{sgn}(n) \sqrt{|n|\Delta^2 + M_\pm^2} & (n = \pm 1, \pm 2, \dots) \end{cases}. \quad (24)$$

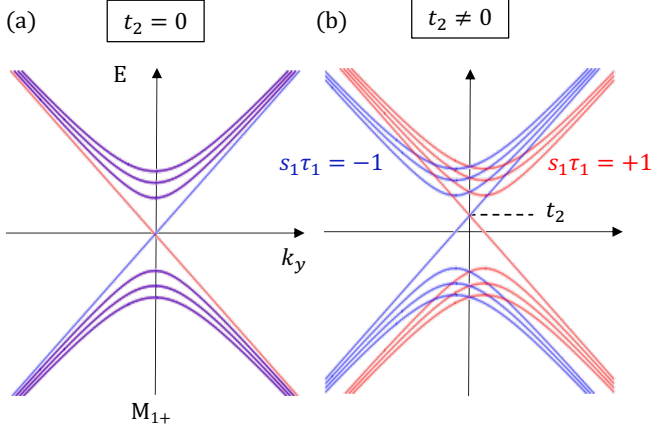


FIG. 7: Band dispersion of the effective Landau levels of Eq. (24) as a function of k_y for (a) $t_2 = 0$ and (b) $t_2 \neq 0$. The red and blue lines represent $s_1\tau_1 = \pm 1$ sectors, respectively.

By using the mapping of Table I, we have

$$M_{\pm} = 2t_2 \mp vk_y, \quad \Delta = \sqrt{4t_0 v q_{\theta}}. \quad (25)$$

This perfectly explains the band structures of the twisted 3DTIs in the small twist angle limit [Fig. 5]. The flatness in k_x direction corresponds to the fact that Landau level is dispersionless. On the other hand, the band disperses in k_y direction because k_y corresponds to the mass parameter M_{\pm} in the Landau level picture. In Fig. 7, we plot the band energy of Eq. (24) as a function of k_y for (a) $t_2 = 0$ and (b) $t_2 \neq 0$, with $t_3 = 0$. The red and blue lines represent the eigenenergies of $s_1\tau_1 = \pm 1$ sectors, respectively. Importantly, the zeroth Landau levels $E_{0,\pm} = M_{\pm}$ are always linear in k_y with the band velocity $\mp v$ (the original band velocity of the surface Dirac cone) regardless of other parameters. If t_2 is switched on, all the energy bands in $s_1\tau_1 = \pm 1$ sectors horizontally shift by $\pm 2t_2/v$ because $M_{\pm} = 2t_2 \mp vk_y$. The off-diagonal element t_3 hybridizes $s_1\tau_1 = \pm 1$ sectors, while never splits double degeneracy at $k_y = 0$ because it is the Kramer's doublet in the original system. These results are consistent with the numerical results in Fig. 5.

Since $q_{\theta}(\propto \theta)$ corresponds to $2\pi\phi$ in Table I, a larger twist angle in the 3DTI interface corresponds to a greater magnetic field in the effective lattice model. In the band structure of the twisted 3DTIs [Fig. 5], indeed, the Landau level spacing increases when q_{θ} is increased. We also note that these flat levels only appear in an energy range of $|E| < 2t_0$. This is understood by a finite depth of the Dirac cone in the effective lattice model, Eq. (18), where the Fermi circle is closed only in $|E| < 2t_0$. When the magnetic flux is too large, the Landau levels get broadened as seen in Figs. 5(a)(b), because of a magnetic breakdown beyond the barrier of $2t_0$. The condition is given by $\Delta \gtrsim 2t_0$, or, equivalently, $vq_{\theta} \gtrsim t_0$. Conversely, the condition for the formation of perfect 1D channels is

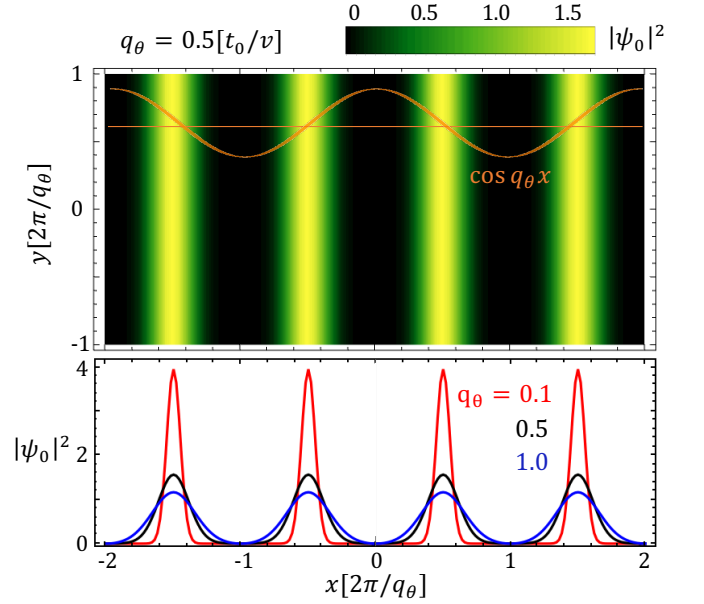


FIG. 8: The square amplitude of a wavefunction in the zeroth level on the twisted TI interface with $t_2 = t_3 = 0$. The upper panel is a density plot on xy -plane for $q_{\theta} = 0.5[t_0/v]$, where the orange curve represents $\cos q_{\theta}x$. The lower panel shows one-dimensional plot against x for $q_{\theta} = 0.1, 0.5, 1.0[t_0/v]$.

given by

$$vq_{\theta} \lesssim t_0, \quad (26)$$

which agrees well with the numerical band calculation in Fig. 5.

C. Wavefunction of zeroth modes

The wavefunctions of pseudo-LL states have highly anisotropic nature in the real space, in accordance with the perfectly one-dimensional energy dispersion. In Fig. 8, we plot the square amplitude of a wavefunction in the zeroth level on the twisted TI interface, where $t_2 = t_3 = 0$ is assumed for simplicity. The wavefunction exhibits a stripe pattern, which is extended in y -direction while localized in x direction. The center coordinates of the stripes are corresponding to the positions where the interlayer matrix $T_{\pm}(\mathbf{r}) \propto t_0 \cos \mathbf{q}_{\theta} \cdot \mathbf{r}$ vanishes. The spacing of the stripes is given by $l_{\text{spc}} = \pi/q_{\theta}$, which is proportional to the moiré period. Owing to the pseudo-Landau level description, the wavefunctions in x direction are well approximated by $|\psi_0| \sim e^{-x^2/(2l_B^2)}$, where

$$l_B = \sqrt{\frac{v}{2t_0 q_{\theta}}} \quad (27)$$

is the effective magnetic length. The l_B is obtained by using an expression $\pi_b = [i/(\sqrt{2}l_B)](a^{\dagger} - a)$ in Eq. (22), and the parameter correspondence in Table I. The width

of the stripe is estimated by the FWHM (full width at half maximum) of $e^{-x^2/(2l_B^2)}$, which is $2\sqrt{2\log 2}l_B \equiv l_w$. The ratio of the stripe width to the stripe spacing is $l_w/l_{\text{spc}} = [2\sqrt{\log 2/\pi}]\sqrt{vq\theta/t_0}$. The condition that the 1D channels are spatially separated, $l_w \lesssim l_{\text{spc}}$, is equivalent to Eq. (26).

The wavefunction of the zeroth level also has a peculiar spin structure. According to Eqs. (20) and (23), the eigenfunction for $n = 0$ Landau levels in $s_1\tau_1 = \pm 1$ sectors have the form of $\psi_{0,+} \propto (1, 0, 0, 0)$ and $\psi_{0,-} \propto (0, 0, 1, 0)$, which correspond to \mathbf{u}_1^+ and \mathbf{u}_1^- , respectively, in the original representation before the unitary transformation [Eq. (19)]. The \mathbf{u}_1^{\pm} is fully spin-polarized in the $\pm s_2$ direction on the upper TI surface (1st and 2nd components), and in the $\mp s_2$ direction on the lower TI surface (3rd and 4th components). Since s_2 corresponds to s_1 in the original spin axis [Eq. (14)], the actual spin-polarization direction is along $\pm x$, which is parallel to the energy contour of the 1D surface band. Since $s_1\tau_1 = \pm 1$ have opposite propagating directions, we conclude that zeroth 1D interface modes in twisted 3DTIs have counter-propagating spin currents on the upper and lower surfaces as schematically illustrated in Fig. 1. Because of the opposite spin configurations, the left-going and right going 1D modes of $n = 0$ are never hybridized by spin-independent scatters. When the Fermi level lies in the zeroth level, therefore, the system is equivalent to a parallel array of independent 1D channels free from the impurity scattering.

We expect that perfect 1D state is experimentally feasible in realistic materials. Let consider SnTe as an example of M-centered 3DTI. The parameters are given by $v = 0.9 \times 10^6$ m/s, $t_0 = 0.2$ eV and lattice constant $a = 0.6$ nm [43, 63–65]. The wavenumber $q\theta$ [Eq. (13)] is given by $[2\pi/(\sqrt{3}a)]\theta$. The condition for the 1D channel formation, Eq. (26), then becomes $\theta \lesssim 3^\circ$. The width of the 1D channel is $2\sqrt{2\log 2}l_B \approx (9/\sqrt{\theta^\circ})\text{nm}$ [Eq. (27)], and the spacing is $\pi/q\theta \approx (30/\theta^\circ)\text{nm}$. Note that v in the equations is replaced with $\hbar v$ in above estimations.

The well-separated, nanometer-scale 1D channel may exhibit Luttinger liquid behavior [66–71]. In the literature, arrays of parallel weakly-coupled Luttinger liquid have been extensively investigated to study non-Fermi liquids in high dimensions [46–50], exotic quantum Hall states [51–53], topological phases [54, 55] and quantum spin liquids [56, 57]. In our twisted 3DTI system, the coupling between 1D channels can be tuned by the twisted angle, and it is expected to be an ideal platform to realize these novel quantum phenomena.

IV. CONCLUSION

We have studied the electronic structure of interface states of twisted 3DTIs. In the case of side-centered 3DTI, the surface Dirac cones are hybridized by a one-dimensional interface coupling with a single moiré wave number, resulting in an array of nearly-

independent one-dimensional channels. The two zeroth levels have counter-propagating spin currents free from spin-independent impurity scattering. The one-dimensional states can be interpreted as Landau levels of the effective lattice model, where the magnetic field corresponds to the twist angle. The coupling amplitude between the neighboring 1D channels can be controlled by the twist angle, and the system would serve as a platform for weakly-coupled parallel Luttinger liquid.

Acknowledgments

This work was supported in part by JSPS KAKENHI Grant Number JP21H05236, JP21H05232, JP20H01840, JP20H00127, and JP20K14415 and by JST CREST Grant Number JPMJCR20T3, Japan. M.F. was supported by a JSPS Fellowship for Young Scientists. The numerical calculations were performed on XC40 at YITP in Kyoto University.

Appendix A: Derivation of the form of Dirac cone

Here, we derive Eq. (2), the Dirac Hamiltonian of surface mode on 3DTI in the presence of the mirror symmetry \mathcal{M}_x and \mathcal{M}_y . A general 2×2 Hamiltonian linear in wavenumber (k_x, k_y) is written as

$$H(\mathbf{k}) = \sum_{\nu=0,3} a_{x,\nu} s_\nu k_x + \sum_{\nu=0,3} a_{y,\nu} s_\nu k_y, \quad (\text{A1})$$

where s_1, s_2, s_3 are Pauli matrices for spin degree of freedom and s_0 is a 2×2 unit matrix, and $a_{i,\nu}$ ($i = x, y$) are real numbers.

Since the 3DTI has the time reversal symmetry, we have

$$\mathcal{T}H(\mathbf{k})\mathcal{T}^{-1} = H(-\mathbf{k}), \quad (\text{A2})$$

where $\mathcal{T} = is_2\mathcal{K}$, where \mathcal{K} and the complex conjugate operator. This immediately gives $a_{x,0} = a_{y,0} = 0$. Time reversal symmetry protects the double degeneracy of surface Dirac cone and it can emerge only at a TRIM.

We assume that the system has both of the mirror-reflection symmetries of \mathcal{M}_x (with respect to yz plane) and \mathcal{M}_y (zx plane). The operators are expressed as $\mathcal{M}_x = is_1$ and $\mathcal{M}_y = is_2$. The \mathcal{M}_x requires

$$\mathcal{M}_x H(\mathbf{k}) \mathcal{M}_x^{-1} = H(\mathcal{M}_x \mathbf{k}), \quad (\text{A3})$$

resulting in $a_{x,1} = a_{y,2} = a_{y,3} = 0$. The \mathcal{M}_y requires

$$\mathcal{M}_y H(\mathbf{k}) \mathcal{M}_y^{-1} = H(\mathcal{M}_y \mathbf{k}), \quad (\text{A4})$$

giving $a_{x,1} = a_{x,3} = a_{y,2} = 0$. If the system has both \mathcal{M}_x and \mathcal{M}_y , only $a_{x,2}$ and $a_{y,1}$ can remain non zero, and therefore the Hamiltonian can be written in a form of

$$H = v_x s_2 k_x - v_y s_1 k_y, \quad (\text{A5})$$

which is Eq. (2).

Appendix B: M-point 3DTI with \mathcal{T} and \mathcal{M}_x or \mathcal{M}_y

In the main part of the paper, we assume the 3DTI before stacking has both \mathcal{M}_x and \mathcal{M}_y , to show the side-centered surface Dirac cone becomes 1D channels in a twisted 3DTI. However, most of real topological insulators actually have lower spatial symmetry. For example, the SnTe (111) surface, which hosts the BZ side-centered Dirac cone, has \mathcal{M}_x symmetry while no \mathcal{M}_y [43–45]. In this appendix, we consider 3DTIs with side-centered surface Dirac cones, which have *either* of \mathcal{M}_x or \mathcal{M}_y , to demonstrate the 1D interface states still exist.

In each case, we construct twisted 3DTIs in the same manner as in Fig. 2. We flip one slab and stack it on the top of the other, so that two slabs share the same mirror plane (yz-plane for \mathcal{M}_x and zx-plane for \mathcal{M}_y). Then we twist the top and bottom slabs with respect the z-axis by $\pm\theta/2$, respectively. The entire system has $\mathcal{C}_{2x}(\mathcal{C}_{2y})$ if the slab has $\mathcal{M}_x(\mathcal{M}_y)$.

1. \mathcal{T} and \mathcal{M}_x

We consider the case where the 3DTI slab has \mathcal{T} and \mathcal{M}_x . This applies to SnTe (111) surface. From the symmetry constraints \mathcal{T} [Eq. (A2)] and \mathcal{M}_x [Eq. (A3)], the surface Dirac Hamiltonian $H_{u/l}$ is written in the lowest order in k as

$$H_{u/l} = \pm[(a_{x2}s_2 + a_{x3}s_3)k_x + a_{y1}s_1k_y]. \quad (\text{B1})$$

where \pm correspond to u and l , respectively. If we rotate the spin axis on s_2 - s_3 plane, we can make the spin texture lie on a s_1 - s_2 plane and the Dirac Hamiltonian become the same form of Eq. (A5).

Now the interface-coupling Hamiltonian takes the form of $H_{\text{int}}^{(M_1)} = T_+e^{iq_\theta \cdot \mathbf{r}} + T_-e^{-iq_\theta \cdot \mathbf{r}}$ as argued in Sec. II. By requiring that the twist 3DTI model respects \mathcal{T} and \mathcal{C}_{2x} , the interlayer Hamiltonian Eq. (6) is reduced to

$$T_\pm = t_0s_0 + (\pm t_2 + it'_2)s_2 + (\pm t'_3 + it_3)s_3, \quad (\text{B2})$$

where t'_2 and t'_3 are real numbers. Note that the general form of the interface Hamiltonian does not change in the spin rotation on s_2 - s_3 plane argued above.

Here, we investigate the effect of t'_2 and t'_3 which are not discussed in Sec. III A. In the following, we assume an isotropic surface Dirac cone $v_x = v_y (\equiv v)$ for simplicity. By diagonalizing Eq. (11), we numerically calculate the energy bands of the twisted 3DTIs with the surface Dirac cone at M_1 . The band structures for nonzero t'_2 and t'_3 are plotted in Fig. 9(b) and (c), respectively, with $q_\theta = 0.25(t_0/v)$. We observe that t'_2 hardly changes the entire band structure, while t'_3 splits the double degeneracy in $k_y \neq 0$. If we consider the pseudo-Landau mapping, the corresponding Hamiltonian to Eq. (20) is given as

$$\begin{pmatrix} h_+ & 2it_3k_a\sigma_2 - 2it'_3\sigma_2 \\ -2it_3k_a\sigma_2 + 2it'_3\sigma_2 & h_- \end{pmatrix}, \quad (\text{B3})$$

with

$$\begin{aligned} h_\pm &= -2t_0k_a\sigma_1 + 2t_bk_b\sigma_2 + M_\pm\sigma_3, \\ M_\pm &= 2t_2 - 2t'_2k_a \pm t_c. \end{aligned} \quad (\text{B4})$$

The t'_2 is coupled with k_a so that the Dirac cone of h_\pm is unchanged in the vicinity of $k_a = 0$. The t'_3 hybridizes $s_1\tau_1 = \pm 1$ sectors just as t_3 does. These results are consistent with the numerical calculations in Fig. 9. Therefore, the 1D flat bands are expected to be observed in the twisted stack of 3DTI having \mathcal{M}_x only, such as SnTe (111) surface.

2. \mathcal{T} and \mathcal{M}_y

We assume that the bulk of nontwisted 3DTI has \mathcal{T} and \mathcal{M}_y , resulting in \mathcal{T} and \mathcal{C}_{2y} for the twisted 3DTIs. From the symmetry constraints \mathcal{T} [Eq. (A2)] and \mathcal{M}_y [Eq. (A4)], the surface Dirac Hamiltonian $H_{u/l}$ is written in the lowest order in k as

$$H_{u/l} = \pm a_{x2}s_2k_x \pm (a_{y1}s_1 + a_{y3}s_3)k_y. \quad (\text{B5})$$

where \pm are for u and l . If we rotate the spin axis on s_1 - s_3 plane, the spin texture lies on a plane and the Dirac Hamiltonian become the same form of Eq. (A5).

The interface-coupling Hamiltonian takes the form of $H_{\text{int}}^{(M_1)} = T_+e^{iq_\theta \cdot \mathbf{r}} + T_-e^{-iq_\theta \cdot \mathbf{r}}$ as argued in Sec. II. By requiring that the twist 3DTI model respects \mathcal{T} and \mathcal{C}_{2y} , the interlayer Hamiltonian Eq. (6) is reduced to

$$T_\pm = t_0s_0 + it_1s_1 \pm t_2s_2 + it_3s_3, \quad (\text{B6})$$

where t_1 is real number. Again, the general form of the interface Hamiltonian does not change in the spin rotation on s_1 - s_3 plane.

We investigate the effect of t_1 which is not discussed in Sec. III A. In the following, we assume an isotropic surface Dirac cone $v_x = v_y (\equiv v)$ for simplicity. The band structure of the twisted 3DTIs with nonzero t_1 in Fig. 9(a) with $q_\theta = 0.25(t_0/v)$. The energy spectrum in Fig. 5(c) is not modified by the t_1 . It can be understood by considering the pseudo-Landau mapping, where t_1 is included in Eq. (21) as

$$\begin{aligned} h_\pm &= -2t_0k_a\sigma_1 + 2(t_bk_b \pm t_1)\sigma_2 + M_\pm\sigma_3, \\ M_\pm &= 2t_2 \pm t_c, \end{aligned} \quad (\text{B7})$$

We see t_1 just shifts the origin of k_b (corresponding to k_x), and hence the 1D bands remain intact.

3. Anisotropic surface Dirac cones

The surface Dirac cone at M point (BZ side center) is generally anisotropic, i.e., $v_x \neq v_y$. This is because the rotation symmetry C_n ($n \geq 3$) is absent in a set of spatial transformations to keep the M point invariant. Here, we calculate the moiré band structure for the

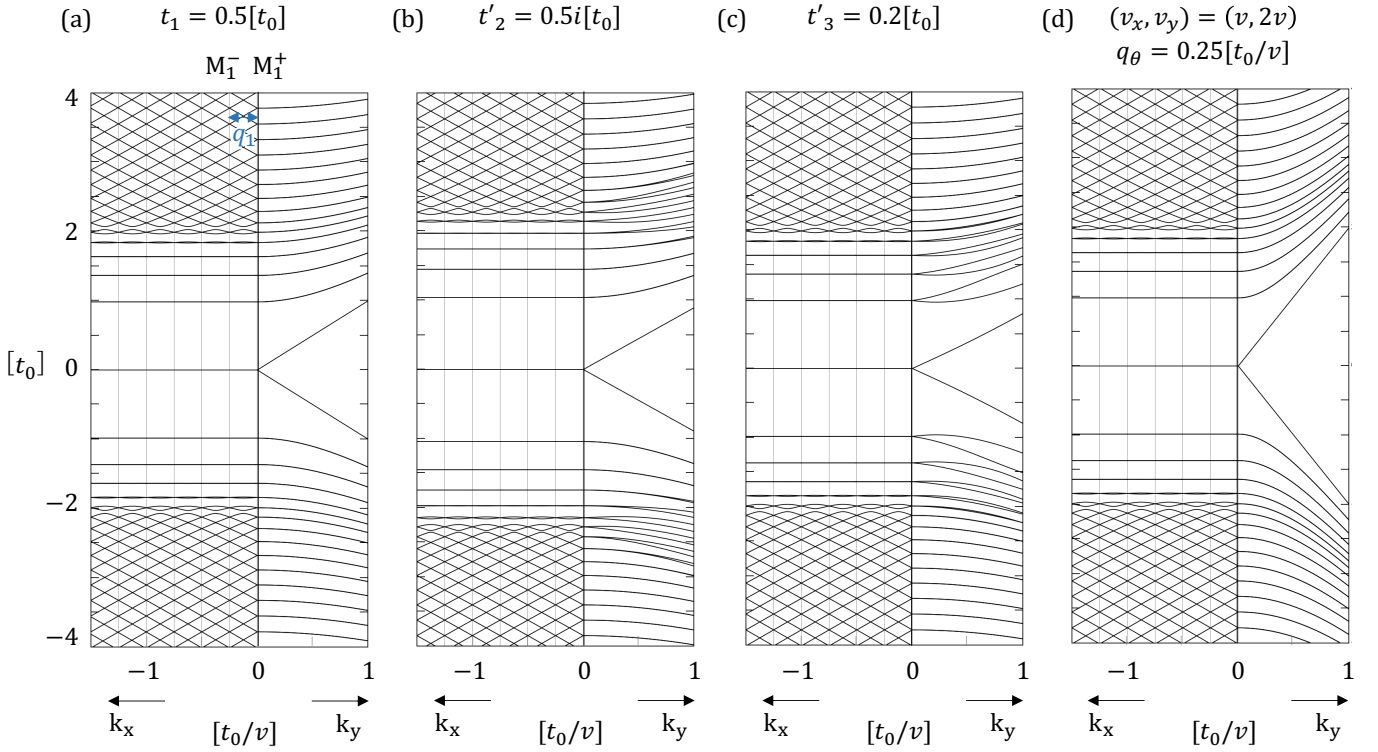


FIG. 9: Plots similar to Fig. 5(c) for (a) $t_1/t_0 = 0.5$, (b) $t'_2/t_0 = 0.5$ and (c) $t'_3/t_0 = 0.2$. (d) The band structure for the anisotropic Dirac cone at M_1 with $(v_x, v_y) = (v, 2v)$ and $q_\theta = 0.25(t_0/v)$.

anisotropic surface Dirac cone. For simplicity we assume the interface Hamiltonian as $H_{\text{int}}^{(M_1)} = t_0 s_0 \cos(q_\theta x)$. Figure 9(d) shows the band structure for $(v_x, v_y) = (v, 2v)$ and $q_\theta = 0.25(t_0/v)$. Compared to Fig. 5(c), the en-

ergy spectrum along k_x axis is completely same while the band velocity along k_y axis becomes twice. Therefore the formation of 1D interface states is not affected by an anisotropy of the surface Dirac cone.

-
- ¹ Z. Li, J. Zhuang, L. Chen, Z. Ni, C. Liu, L. Wang, X. Xu, J. Wang, X. Pi, X. Wang, et al., ACS Cent. Sci. **2**, 517 (2016).
 - ² P.-C. Yeh, W. Jin, N. Zaki, J. Kunstmann, D. Chenet, G. Arefe, J. T. Sadowski, J. I. Dadap, P. Sutter, J. Hone, et al., Nano Lett. **16**, 953 (2016).
 - ³ Q. Tong, H. Yu, Q. Zhu, Y. Wang, X. Xu, and W. Yao, Nat. Phys. **13**, 356 (2017).
 - ⁴ M. H. Naik and M. Jain, Phys. Rev. Lett. **121**, 266401 (2018).
 - ⁵ J. Y. Lee, E. Khalaf, S. Liu, X. Liu, Z. Hao, P. Kim, and A. Vishwanath, Nat. Commun. **10**, 1 (2019).
 - ⁶ X. Liu, Z. Hao, E. Khalaf, J. Y. Lee, Y. Ronen, H. Yoo, D. Haei Najafabadi, K. Watanabe, T. Taniguchi, A. Vishwanath, et al., Nature **583**, 221 (2020).
 - ⁷ C. Shen, Y. Chu, Q. Wu, N. Li, S. Wang, Y. Zhao, J. Tang, J. Liu, J. Tian, K. Watanabe, et al., Nat. Phys. **16**, 520 (2020).
 - ⁸ B. Lian, Z. Liu, Y. Zhang, and J. Wang, Phys. Rev. Lett. **124**, 126402 (2020).
 - ⁹ A. Weston, Y. Zou, V. Enaldiev, A. Summerfield, N. Clark, V. Zolyomi, A. Graham, C. Yelgel, S. Magorrian, M. Zhou, et al., Nat. Nanotechnol. **15**, 592 (2020).
 - ¹⁰ M. R. Rosenberger, H.-J. Chuang, M. Phillips, V. P. Oleshko, K. M. McCreary, S. V. Sivaram, C. S. Hellberg, and B. T. Jonker, ACS Nano **14**, 4550 (2020).
 - ¹¹ L. Wang, E.-M. Shih, A. Ghiotto, L. Xian, D. A. Rhodes, C. Tan, M. Claassen, D. M. Kennes, Y. Bai, B. Kim, et al., Nat. Mater. **19**, 861 (2020).
 - ¹² D. M. Kennes, L. Xian, M. Claassen, and A. Rubio, Nat. Commun. **11**, 1124 (2020).
 - ¹³ M. Fujimoto and T. Kariyado, Phys. Rev. B **104**, 125427 (2021).
 - ¹⁴ J. An and J. Kang, J. Phys. Chem. Lett. **12**, 12283 (2021).
 - ¹⁵ Z.-X. Luo, C. Xu, C.-M. Jian, et al., Phys. Rev. B **104**, 035136 (2021).
 - ¹⁶ M. He, Y. Li, J. Cai, Y. Liu, K. Watanabe, T. Taniguchi, X. Xu, and M. Yankowitz, Nat. Phys. **17**, 26 (2021).
 - ¹⁷ J. M. Park, Y. Cao, K. Watanabe, T. Taniguchi, and P. Jarillo-Herrero, Nature **590**, 249 (2021).
 - ¹⁸ T. Song, Q.-C. Sun, E. Anderson, C. Wang, J. Qian, T. Taniguchi, K. Watanabe, M. A. McGuire, R. Stöhr, D. Xiao, et al., Science **374**, 1140 (2021).
 - ¹⁹ M. Akram, H. LaBollita, D. Dey, J. Kapeghian, O. Erten,

- and A. S. Botana, *Nano Lett.* **21**, 6633 (2021).
- ²⁰ Y. Xu, A. Ray, Y.-T. Shao, S. Jiang, D. Weber, J. E. Goldberger, K. Watanabe, T. Taniguchi, D. A. Muller, K. F. Mak, et al., arXiv:2103.09850.
 - ²¹ H. Xie, X. Luo, G. Ye, Z. Ye, H. Ge, S. H. Sung, E. Renich, S. Yan, Y. Fu, S. Tian, et al., *Nat. Phys.* **18**, 30 (2022).
 - ²² G. Chaudhary, A. A. Burkov, and O. G. Heinonen, arXiv:2205.00349.
 - ²³ P. Wang, G. Yu, Y. H. Kwan, Y. Jia, S. Lei, S. Klemen, F. A. Cevallos, R. Singha, T. Devakul, K. Watanabe, et al., *Nature* **605**, 57 (2022).
 - ²⁴ Y. Soeda, K. Asaga, and T. Fukui, *Phys. Rev. B* **105**, 165422 (2022).
 - ²⁵ J. M. B. Lopes dos Santos, N. M. R. Peres, and A. H. Castro Neto, *Phys. Rev. Lett.* **99**, 256802 (2007).
 - ²⁶ E. J. Mele, *Phys. Rev. B* **81**, 161405 (2010).
 - ²⁷ G. Trambly de Laissardière, D. Mayou, and L. Magaud, *Nano Lett.* **10**, 804 (2010).
 - ²⁸ S. Shallcross, S. Sharma, E. Kandelaki, and O. A. Pankratov, *Phys. Rev. B* **81**, 165105 (2010).
 - ²⁹ E. Suárez Morell, J. D. Correa, P. Vargas, M. Pacheco, and Z. Barticevic, *Phys. Rev. B* **82**, 121407 (2010).
 - ³⁰ R. Bistritzer and A. H. MacDonald, *Proc. Natl. Acad. Sci. U.S.A.* **108**, 12233 (2011).
 - ³¹ M. Kindermann and P. N. First, *Phys. Rev. B* **83**, 045425 (2011).
 - ³² L. Xian, S. Barraza-Lopez, and M. Y. Chou, *Phys. Rev. B* **84**, 075425 (2011).
 - ³³ J. L. Dos Santos, N. Peres, and A. C. Neto, *Phys. Rev. B* **86**, 155449 (2012).
 - ³⁴ P. Moon and M. Koshino, *Phys. Rev. B* **85**, 195458 (2012).
 - ³⁵ G. Trambly de Laissardière, D. Mayou, and L. Magaud, *Phys. Rev. B* **86**, 125413 (2012).
 - ³⁶ P. Moon and M. Koshino, *Phys. Rev. B* **87**, 205404 (2013).
 - ³⁷ Y. Liu, Y. Li, S. Rajput, D. Gilks, L. Lari, P. Galindo, M. Weinert, V. Lazarov, and L. Li, *Nat. Phys.* **10**, 294 (2014).
 - ³⁸ K. Schouteden, Z. Li, T. Chen, F. Song, B. Partoens, C. Van Haesendonck, and K. Park, *Sci. Rep.* **6**, 1 (2016).
 - ³⁹ T. Wang, N. F. Q. Yuan, and L. Fu, *Phys. Rev. X* **11**, 021024 (2021).
 - ⁴⁰ J. Cano, S. Fang, J. H. Pixley, and J. H. Wilson, *Phys. Rev. B* **103**, 155157 (2021).
 - ⁴¹ I. Tateishi and M. Hirayama, arXiv:2112.13770.
 - ⁴² A. Dunbrack and J. Cano, arXiv:2112.11464.
 - ⁴³ Y. Tanaka, Z. Ren, T. Sato, K. Nakayama, S. Souma, T. Takahashi, K. Segawa, and Y. Ando, *Nat. Phys.* **8**, 800 (2012).
 - ⁴⁴ Y. Shi, M. Wu, F. Zhang, and J. Feng, *Phys. Rev. B* **90**, 235114 (2014).
 - ⁴⁵ J. Wang, J. Liu, Y. Xu, J. Wu, B.-L. Gu, and W. Duan, *Phys. Rev. B* **89**, 125308 (2014).
 - ⁴⁶ X. Wen, *Phys. Rev. B* **42**, 6623 (1990).
 - ⁴⁷ V. J. Emery, E. Fradkin, S. A. Kivelson, and T. C. Lubensky, *Phys. Rev. Lett.* **85**, 2160 (2000).
 - ⁴⁸ S. L. Sondhi and K. Yang, *Phys. Rev. B* **63**, 054430 (2001).
 - ⁴⁹ A. Vishwanath and D. Carpentier, *Phys. Rev. Lett.* **86**, 676 (2001).
 - ⁵⁰ R. Mukhopadhyay, C. Kane, and T. Lubensky, *Phys. Rev. B* **64**, 045120 (2001).
 - ⁵¹ C. Kane, R. Mukhopadhyay, and T. Lubensky, *Phys. Rev. Lett.* **88**, 036401 (2002).
 - ⁵² J. C. Teo and C. Kane, *Phys. Rev. B* **89**, 085101 (2014).
 - ⁵³ P. M. Tam and C. L. Kane, *Phys. Rev. B* **103**, 035142 (2021).
 - ⁵⁴ T. Neupert, C. Chamon, C. Mudry, and R. Thomale, *Phys. Rev. B* **90**, 205101 (2014).
 - ⁵⁵ T. Iadecola, T. Neupert, C. Chamon, and C. Mudry, *Phys. Rev. B* **93**, 195136 (2016).
 - ⁵⁶ T. Meng, T. Neupert, M. Greiter, and R. Thomale, *Phys. Rev. B* **91**, 241106 (2015).
 - ⁵⁷ A. A. Patel and D. Chowdhury, *Phys. Rev. B* **94**, 195130 (2016).
 - ⁵⁸ M. Koshino, *New J. Phys.* **17**, 015014 (2015).
 - ⁵⁹ T. Kariyado and A. Vishwanath, *Phys. Rev. Research* **1**, 033076 (2019).
 - ⁶⁰ D. L. Miller, K. D. Kubista, G. M. Rutter, M. Ruan, W. A. de Heer, P. N. First, and J. A. Stroscio, *Science* **324**, 924 (2009).
 - ⁶¹ G. Li, A. Luican, and E. Y. Andrei, *Phys. Rev. Lett.* **102**, 176804 (2009).
 - ⁶² Y. J. Song, A. F. Otte, Y. Kuk, Y. Hu, D. B. Torrance, P. N. First, W. A. de Heer, H. Min, S. Adam, M. D. Stiles, et al., *Nature* **467**, 185 (2010).
 - ⁶³ P. Dziawa, B. Kowalski, K. Dybko, R. Buczko, A. Szczerbakow, M. Szot, E. Łusakowska, T. Balasubramanian, B. M. Wojek, M. Berntsen, et al., *Nat. Mater.* **11**, 1023 (2012).
 - ⁶⁴ T. H. Hsieh, H. Lin, J. Liu, W. Duan, A. Bansil, and L. Fu, *Nat. Commun.* **3**, 1 (2012).
 - ⁶⁵ Y. Tanaka, T. Shoman, K. Nakayama, S. Souma, T. Sato, T. Takahashi, M. Novak, K. Segawa, and Y. Ando, *Phys. Rev. B* **88**, 235126 (2013).
 - ⁶⁶ S.-i. Tomonaga, *Prog. Theor. Phys.* **5**, 544 (1950).
 - ⁶⁷ J. Luttinger, *J. Math. Phys.* **4**, 1154 (1963).
 - ⁶⁸ F. Haldane, *Phys. Rev. Lett.* **47**, 1840 (1981).
 - ⁶⁹ J. Voit, *Rep. Prog. Phys.* **58**, 977 (1995).
 - ⁷⁰ T. Giamarchi, *Quantum physics in one dimension*, vol. 121 (Clarendon press, 2003).
 - ⁷¹ A. Chang, *Rev. Mod. Phys.* **75**, 1449 (2003).